Journal of Materials Chemistry C

ROYAL SOCIETY OF CHEMISTRY

PAPER

View Article Online
View Journal

Cite this: DOI: 10.1039/d5tc02144h

Flexible high-sensitivity magnetoelectric thin film composites of solution-derived $BiFeO_3$–$PbTiO_3$ layers on Ni foils

Adriana Barreto, [a] Ricardo Jiménez, [a] Pablo Ramos, [b] Harvey Amorín, [a] Íñigo Bretos, [a] Miguel Algueró *[a] and M. Lourdes Calzada *[a]

This study propels the development of high-sensitivity magnetoelectric (ME) thin-film composites for miniaturized energy harvesters, targeting applications like wearable self-powered sensors and actuators. ME structures are fabricated using a low-temperature solution deposition method, which is both cost-effective and straightforward for real device fabrication. The materials consist of $BiFeO_3$–$PbTiO_3$ ferro-piezoelectric perovskite thin films deposited on magnetostrictive nickel (Ni) substrates. For the first time, the study investigates films with sub-micron thickness ($\leq$500 nm) of this high Curie temperature perovskite compound, and compares the performance of rigid and flexible structures. A major challenge was to attain good elastic coupling between the piezoelectric and magnetostrictive components to enhance magnetoelectric responses. A synergistic approach was used to achieve this goal combining low-temperature processing to minimize Ni oxidation and the introduction of a lanthanum manganite ($La_{0.7}Sr_{0.3}MnO_3$, LSMO) layer between the ferroelectric oxide and magnetic metal. The solution-derived LSMO acts simultaneously as a diffusion barrier, bottom electrode and crystallization promoter for the BF–PT film. Flexible structures demonstrate superior functional performance, with high remnant polarizations ($P_R \sim 50$ μC cm^{-2}) and voltage magnetoelectric coefficients ($\alpha_{ME} \sim 100$ mV cm^{-1} Oe^{-1}), as well as appropriate voltage sensitivity to magnetic field ($\sim$3.8 μV Oe^{-1}), demonstrating their suitability for multifunctional energy harvesting and sensing technologies.

Received 2nd June 2025,
Accepted 20th August 2025

DOI: 10.1039/d5tc02144h

rsc.li/materials-c

1. Introduction

The current demand of wireless autonomous electronic devices has pushed the investigation of energy harvesting concepts to realize self-powering. Hence, scavenging of different types of energy is being investigated for application in low-power electronics. Vibrations, magnetic fields, thermal energy, light, water flow and wind are available sources.[1,2] Among them, the use of electromagnetic radiation has strong potential for energy harvesting making use of the magnetoelectric (ME) effect. It consists in the generation of electric polarization (P) upon the application of a magnetic field (H) and *vice versa*.[3] This ME effect can be obtained in composite materials formed by piezoelectric and magnetostrictive phases,[4] and devices are attracting great research interest due to their multifunctionality and potential use in a range of applications besides energy harvesting.[5,6]

The miniaturization of ME devices requires evolving bulk technologies into thin film ones, and it is a major technological trend in the field. Smaller scales allow higher device integration on a single chip, while sensitivity and efficiency when capturing small magnetic stimuli are boosted after downsizing. Therefore, thin film devices can operate from sources inaccessible at larger scales.[7] Today, increasing attention is paid to the design of microelectromechanical systems (MEMS) formed by deposition of ferroelectric films onto metallic substrates. The high fracture strength of metals provides better mechanical performance under large deformations than the conventional stiff and brittle Si substrate. In addition, any ferroelectric film deposited on a magnetic metal is inherently a multiferroic laminate composite capable of providing magnetoelectricity as a product property of the piezoelectricity and magnetostriction of the ferroic components (*i.e.*, the ferroelectric film and the magnetic substrate) through their elastic coupling.[8–11] The performance of these ME heterostructures for sensing and energy harvesting applications is determined by the ME voltage coefficient (α_{ME}) (see the SI and Fig. S1), which is influenced,

[a] *Instituto de Ciencia de Materiales de Madrid, Consejo Superior de Investigaciones Científicas (ICMM-CSIC), C/Sor Juana Inés de la Cruz, Cantoblanco, 28049-Madrid, Spain. E-mail: lcalzada@icmm.csic.es*

[b] *Departamento de Electrónica, Universidad de Alcalá, 28805-Alcalá de Henares, Spain*

among other factors, by the individual properties of the piezoelectric and magnetic materials, the characteristics of the interface between these phases and the volume fraction of the components in the ME heterostructure.[10,12]

Among ferroelectric materials, the most widely used one in these ME heterostructures is high-sensitivity-piezoelectric $Pb(Zr,Ti)O_3$ (PZT) with a perovskite structure and composition at the morphotropic phase boundary (MPB). Here, the coexistence of a rhombohedral and a tetragonal phase results in an enhancement of the ferroelectric and piezoelectric properties. However, despite the high piezoelectric response of PZT, a strong depletion of its functionality is found for nanosize-grained PZT film materials. This is because ferroelectricity is a cooperative phenomenon, and the spontaneous polarization tends to vanish when size decreases across the nanoscale and the number of interacting dipoles reduces.[13]

Regarding the magnetic substrate, nickel (Ni) stands out among base metals as an excellent candidate because it is an inexpensive material with significant magnetostriction.[8,9] Although other magnetic metals have been considered for the fabrication of these ME heterostructures,[10,14] Ni seems to be especially appropriate for inclusion in PZT-based structures because its mechanical impedance is similar to that of PZT ($\sim$27 MRayl). This should facilitate elastic coupling and thus, enhance ME responses. However, achieving an appreciable voltage output (α_{ME}) is challenging because of the thermodynamic incompatibility between PZT and Ni. Ellingham diagrams indicate that there is not a processing window of temperature and pO_2 where the reduction of PbO and the oxidation of Ni do not take place (Fig. S2). This results in the formation of uncontrolled inactive layers between the piezoelectric PZT and the magnetostrictive Ni components that hinder the strain transfer and thus, degrade the ME response. The formation of these detrimental interfaces can be kinetically limited by using low-temperature processes. However, a sharp decrease in grain size, and therefore in properties, is produced when the processing temperature of PZT films is reduced.[15] Besides, lead-free ferroelectric layers would be preferred for new applications, following current enforced regulations aimed at reducing environmental impact and promoting the development of safer, more sustainable electronic materials.[16] Nonetheless, only complex perovskite compositions that are difficult to synthesize are able to achieve piezoelectric coefficients comparable to that of PZT, whose behaviour on down-scaling is even worse than that of PZT.[17] We have found that $BiFeO_3$–$PbTiO_3$ (BFO–PTO) perovskite oxide might provide a trade-off between sustainability and stable properties upon nanostructuring, so it is particularly interesting to be introduced into these heterostructures. This solid solution presents a MPB region where an enhancement of the piezoelectric crystal coefficients is produced, although they do not reach values comparable to those of PZT materials ($^{PZT}d_{33}$ = 400 pC N^{-1} and $^{BFO-PTO}d_{33}$ = 87 pC N^{-1}). However, the MPB region for the BFO–PTO solid solution occurs for compositions around $0.65BiFeO_3$–$0.35PbTiO_3$ (*i.e.*, $Bi_{0.65}Pb_{0.35}Fe_{0.65}Ti_{0.35}O_3$),[18,19] which constitutes a strong reduction in the Pb content as compared with that of the MPB PZT composition ($0.52PbZrO_3$–$0.48PbTiO_3$, *i.e.*, $Pb(Zr_{0.52}Ti_{0.48})O_3$). Another important advantage is that, as compared with PZT, BFO–PTO shows reduced ferroelectric/ferroelastic domain wall activity and high Curie temperature ($T_C \geq 600$ °C, $\sim$300 °C above the T_C of PZT). Consequently, BFO–PTO materials show much more stable functional properties on size reduction. This occurs even when the microstructure is refined across the submicron range down to the nanoscale.[20–22] Therefore, the high stability of the properties in BFO–PTO opens the window to decreasing the processing temperature to minimize Ni oxidation whilst maintaining an appropriate piezoelectric response in the resulting fine-grained BFO–PTO films.

Reducing the processing temperature is not the only strategy to improve the magnetoelectric (ME) response of piezoelectric lead-based perovskite films on Ni substrates.[3,8,23–26] The insertion of conductive barrier layers between the film and Ni could also be explored. In this regard, $LaNiO_3$ perovskite oxide layers have been previously studied due to their ability to play a three-fold role: acting as a buffer barrier, serving as a bottom electrode, and facilitating perovskite nucleation in the film.[9,27–30] Among the potential conductive buffer layers, lanthanum strontium manganite oxide ($La_{0.7}Sr_{0.3}MnO_3$, LSMO) stands out as an appealing alternative layer.[31,32] In addition, it shows room-temperature ferromagnetism, and strong magnetoelectricity was reported in LSMO layers deposited on ferro-piezoelectric perovskite single crystals.[33] It is important to note here that large direct ME responses (polarization/voltage under a magnetic field) are expected for ferro-piezoelectric films on Ni substrates. However, converse ME responses (magnetization under an electric field) are likely to remain small in this geometry, primarily due to the limited strain transfer from the ferroelectric layer to the substrate. Nevertheless, incorporating LSMO layers into this geometry could yield additional effects, potentially enhancing the converse ME response through the material's strongly correlated lattice, electronic, and magnetic properties.[34] Considering these characteristics, we propose the integration of thin LSMO conductive oxide layers into these ME heterostructures as a promising alternative to the traditional $LaNiO_3$ perovskite.

Finally, and in addition to the actual individual components and the interface they form, the volume fraction of the components in the ME heterostructure also has an important effect in the values of α_{ME}. Regarding this aspect, it must be noted that the proposed thin film geometry, even if it avoids clamping effects associated with inactive substrates, is characterized by ferroelectric fractions well below 0.1, far from the thickness ratio for maximum response predicted by theory, which is around 0.5.[10,12] In this low ferroelectric fraction region, the magnetoelectric response increases with the ferroelectric thickness or when the substrate is thinned to obtain flexible structures. Note that the typical design for harvesting is the ME cantilever heterostructure,[35] in which the piezoelectric film is deposited on a magnetic metal foil.[8,9,22,28] These ME devices can operate at low resonance frequencies with high sensitivity, sensing magnetic signals with high spatial resolution or

scavenging energy just from tiny or stray ambient vibrations or human body motions.

In this work, we have addressed the fabrication of high-sensitivity magnetoelectric composites based on this thin-film geometry, considering the different aspects to optimize response. Firstly, the ferroelectric BFO–PTO perovskite with a composition in the MPB was selected, instead of the classical PZT, due to the previously related benefits that this piezoelectric compound offers at the nanoscale. Secondly, the characteristics of the interface between the BFO–PTO film and Ni substrate have been intentionally altered either by kinetically controlling the nickel oxidation by means of low-temperature solution deposition processes or by the introduction of a conductive buffer layer of the LSMO perovskite. Specifically, low-temperature solution processes with a low carbon footprint and low energy consumption have been used for the direct and large-area deposition of the BFO–PTO perovskite layers on the magnetic Ni substrates, taking advantage of the progress made by our group in the fabrication of ferroelectric films by these methods.[15,36–40] Finally, the effects of the thickness of the Ni substrate on the piezoelectric BFO–PTO film and the magnetoelectric response of this system have been studied. Substrates with decreasing thickness were used, so that an evolution from rigid to flexible structures was naturally obtained. The combination of low temperature processing, the use of an interfacial LSMO buffer and the substrate thinning to achieve flexibility has allowed us to optimize the ME response of ferroelectric BFO–PTO films on magnetic Ni substrates, showing these materials to be potential candidates for miniaturized energy harvesters and flexible sensing devices.

2. Results and discussion

As illustrated in Fig. 1, two heterostructural designs were investigated for obtaining magnetoelectric (ME) thin film devices in this study. The schematic shown in Fig. 1a depicts the conventional configuration where a BFO–PTO ferro-piezoelectric thin film is directly solution-deposited onto Ni substrates with decreasing thickness. The formation of a nickel oxide layer is reckoned to be unavoidable despite using relatively low-temperature solution processing (Fig. S2–S4). This configuration is fundamental in understanding the basic interactions and limitations of direct solution deposition methods. The second configuration, shown in the schematic of Fig. 1b, introduces a more complex design where a LSMO buffer conductive layer is previously deposited onto the metal substrate, also by a low-temperature CSD method.

Some nickel oxidation is anticipated too, though it is not expected to affect electrical performance in this configuration since LSMO works here as a bottom electrode. Besides, LSMO has a perovskite crystal structure with cell parameters close to those of many ferro-piezoelectric perovskites, such as BFO–PTO.[41] This structural compatibility helps the nucleation of the perovskite film facilitating the formation of the desired perovskite phase in the subsequent processing stages. Moreover, the lattice matching between the LSMO layer and the ferro-piezoelectric BFO–PTO film reduces film strain and dislocations. Studies have shown that in-plane strains can modify the position of the morphotropic phase boundary (MPB), which must be carefully controlled for enhancing the piezoelectric response of these thin film materials. Therefore, this additional

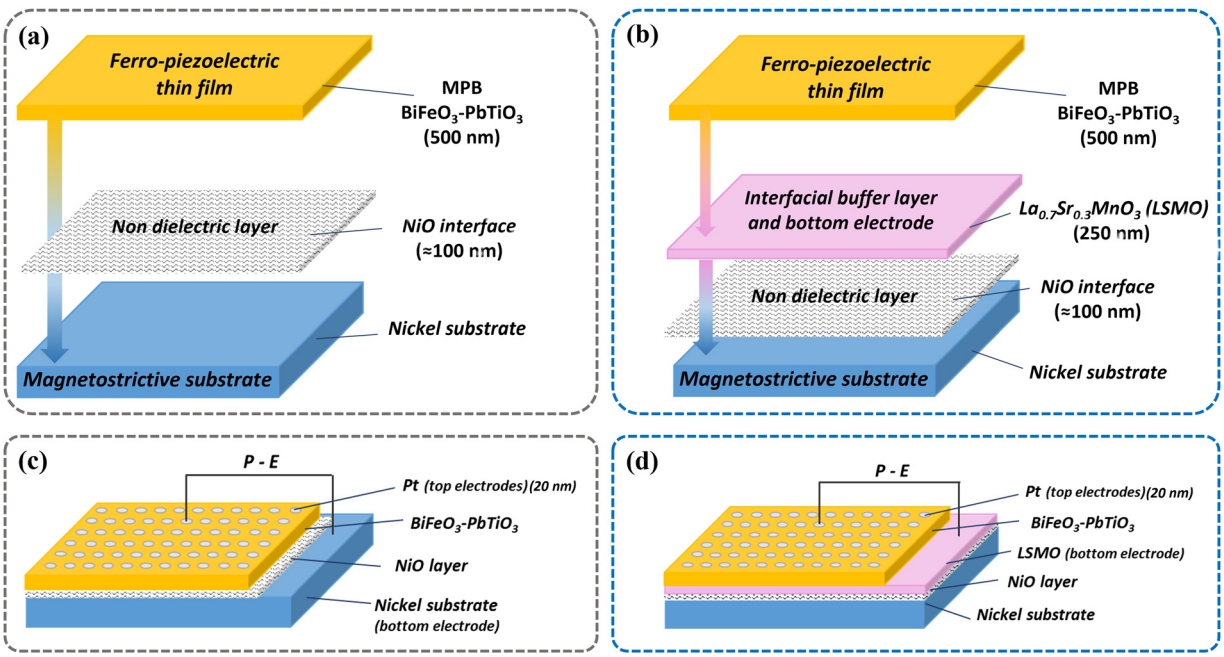

Fig. 1 Schematic diagrams of the magnetoelectric devices. Structure comprising a ferro-piezoelectric thin film (MPB $BiFeO_3$–$PbTiO_3$) directly deposited by CSD on (a) a Ni substrate and (b) a LSMO buffered Ni substrate. Panels (c) and (d) show how electrical contacts are integrated in the final capacitor device.

LSMO layer aims at mitigating many of the observed issues related with the direct solution deposition of films, as well as at providing a bottom electrode, so that an enhanced ME response could result from an optimized ferroelectric polarization of the film. In the detailed views of Fig. 1c and d, the electrical contacts in the fabricated capacitor devices are shown. The left schematic shows the case of the BFO–PTO film directly deposited on Ni. In this case, the capacitor stack includes a NiO layer formed by the natural oxidation of the surface of the Ni substrate during the film processing. This issue increases the resistance, thereby compromising the ferroelectric behavior of the device. In contrast, the right schematic highlights the improved configuration designed in this work, where the electric contact is directly made on the LSMO conductive buffer layer, thus avoiding the detrimental effect of the NiO layer, whose formation is reckoned unavoidable during the fabrication of the capacitor device (SI, Fig. S2).

The synchrotron X-ray radiation diffraction (SXRD) patterns collected with variable incidence angle (2.5° and 5°) for the MPB BFO–PTO ($0.65BiFeO_3$–$0.35PbTiO_3$) films directly deposited on Ni are compared with those for the films deposited onto the LSMO buffered Ni substrates in Fig. 2a and b. The patterns in the figure correspond to films deposited on a rigid Ni plate (700 μm-thick Ni substrate). Analogous results were obtained for those films on 38 μm thick Ni foils (Fig. S5). For the films directly deposited on Ni, perovskite polymorphic phase coexistence is observed from the XRD patterns with a predominant rhombohedral symmetry and a minor, yet distinctive tetragonal phase. A bismuth-rich ternary bismuth iron oxide secondary phase (JCPDS 46-0416), is detected in a lower proportion. In addition, reflections corresponding to nickel oxide (NiO) (JCPDS 04-0835) are observed in this pattern. On the other hand, for the films deposited on the LSMO-coated Ni substrates (LSMO/Ni), the presence of LSMO seems to hinder the formation of the secondary bismuth-rich ternary bismuth iron oxide phase. This likely reflects the perovskite seeding effect of the LSMO buffer coating, facilitating the nucleation of the BFO–PTO perovskite film. Phase coexistence seems not to be the same in the two samples because the tetragonal phase is not observed in the film deposited on LSMO/Ni. It should be noted that the MPB is placed at $x \sim 0.35$ for bulk materials, and a shift to higher x-values has been observed in films, which is

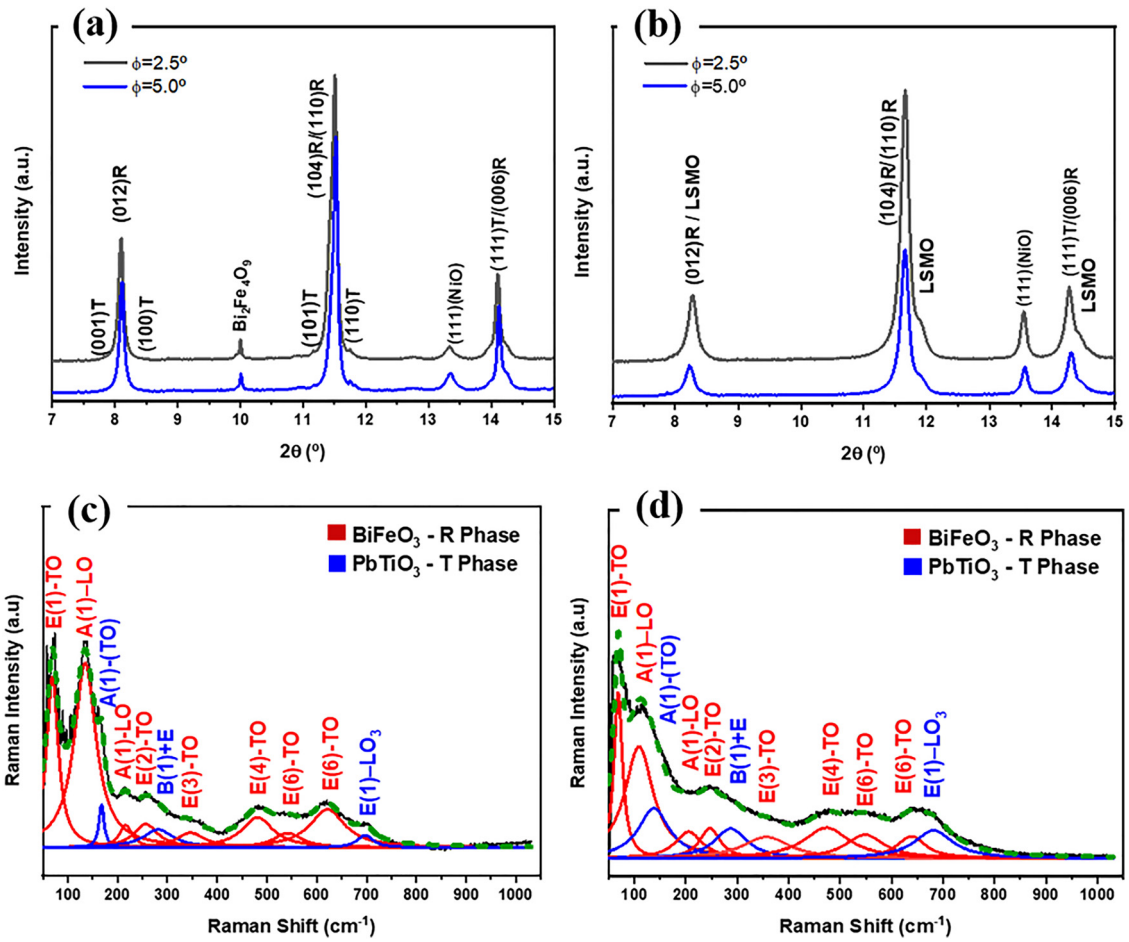

Fig. 2 Grazing-incidence X-ray synchrotron diffraction (XRD) patterns of the MPB BFO–PTO films directly deposited on (a) 700 μm thick Ni substrates and (b) LSMO buffered 700 μm thick Ni substrates. Gaussian fitting Raman spectra and labelled vibration modes of the MPB BFO–PTO films directly deposited on (c) 700 μm thick Ni substrates and (d) LSMO buffered 700 μm thick Ni substrates.

associated with in-plane strain.[42,43] Therefore, large stresses would exist in both film samples, although they seem to be partially relaxed for the film deposited on Ni.

Raman spectra of these thin film samples are shown in Fig. 2c and d. They were obtained in the range of 50–1000 cm^{-1}. Penetration depth D_p is calculated as $D_p = \lambda/4\pi k$, where λ stands for the laser radiation wavelength and k is the film extinction coefficient. A value of 250 nm is estimated for λ = 532 nm using k = 0.16 based on literature data.[44,45] Consequently, in the Raman measurements of these films, LSMO vibration modes are not visible in the spectra because they are located beneath a ~500 nm BFO–PTO layer, beyond the calculated penetration depth. It should be considered that Raman scattering is very sensitive to point group symmetry, making it a valuable complementary technique to XRD analysis. The Raman spectra of the BFO–PTO thin films directly deposited on Ni and on LSMO/Ni (Fig. 2c and d), confirm the perovskite polymorphic phase coexistence, revealing the presence of both rhombohedral and tetragonal phases in both samples. While the XRD data provides an average crystal structure and thus, it primarily detects dominant phases with a long-range order, XRD is not sensitive to possible additional short-range lattice ordering. In contrast, Raman scattering is highly sensitive to local symmetry, enabling subtle or minor short-ranged phases to be uncovered. This might be the case for the films on LSMO/Ni, for which phase coexistence could now be revealed in the Raman spectra but not in the XRD patterns in Fig. 2b and d.

According to group theory analysis, 13 Raman-active modes classified as 4 A_1 and 9 E modes are expected for the rhombohedral $BiFeO_3$ phase with R_{3c} symmetry.[46] Specifically, the modes at 132 cm^{-1} and 213 cm^{-1} detected in the spectra correspond to the longitudinal optical phonons with A_1 symmetry [A_1(LO)]. In addition, those detected at 72, 258, 342, 477, 535, and 621 cm^{-1} are attributed to the transverse optical phonons with E symmetry [E(TO)].[47,48] Meanwhile, in the $PbTiO_3$ tetragonal phase, which has C_{4v} symmetry, each of the T_{1u} modes splits into A_1 and E symmetries, while the T_{2u} mode transforms as B_1 + E. Due to long-range electrostatic forces, the A_{1A} and E modes are further split into transverse optical (TO) and longitudinal optical (LO) modes. Although this effect is expected in B_1 + E modes, it is not typically observed, being active in the B_1, A_{1A} and E Raman modes.[49] For the films in this study, the mode at 155 cm^{-1} is observed, which corresponds to the transverse optical phonons with A_1 symmetry [A_1(TO)]. In addition, the peaks detected at 278 cm^{-1} (B_1 + E) and 692 E(LO_3) cm^{-1} are attributed to the longitudinal optical phonons with E symmetry.[50] These assignments are highlighted in Fig. 2c and d. All the Raman spectra for the two sets of samples with and without LSMO buffer layer are collected in Fig. S6. Therefore, and complementing the obtained results by XRD (Fig. 2a and b), where the tetragonal structure was not detected in the films on the LSMO/Ni substrates, the Raman study is able to distinguish the presence of the rhombohedral and tetragonal phases in both types of film composites (with/without LSMO layer) (Fig. 2c and d). This suggests the presence of tetragonal domains, which might be associated with a hierarchical structure of nanosized tetragonal distortions embedded into larger rhombohedral domains, typical in MPBs, but also alternatively to its presence at the relaxed surface layer of the BFO–PTO film that would be thinner for the film on LSMO/Ni than that on Ni.[51]

The experimentally measured current *vs.* electric field loops, *J–E*, and the corresponding ferroelectric *P–E* hysteresis, measured at room temperature (RT) for the BFO–PTO films on the different Ni substrates with/without the LSMO layer are displayed in Fig. 3. Results for films deposited on the Ni-substrates with different thickness (38 and 700 μm) (Fig. 3a and b) are presented with the aim to elucidate its role in functionality, as well as to assess the feasibility of fabricating flexible structures. Typically, these measurements have to be conducted below RT for BFO-derived materials to minimize leakage current effects, as they lead to energy dissipation and reduce the effectiveness of the applied electric field to switch ferroelectric domains.[52] However, ferroelectric hysteresis loops can be measured in these films at RT, because of their comparatively lower leakage currents, thus showing a robust ferroelectric behavior at ambient conditions necessary for applications. Ferroelectric switching is observed for all films. However, and compared with the values of remnant polarization reported for BFO–PTO films on conventional Pt-coated Si substrates,[53] a low switched polarization was obtained for the films directly deposited on Ni. This is thought to be due to the NiO interlayer formed between the Ni metal substrate and the ferroelectric BFO–PTO film during annealing of the samples (Fig. S2). This configuration divides the applied electric field across the capacitor between the NiO interface and the ferroelectric film, with each layer experiencing a fraction of the total field based on their distinct dielectric properties. Consequently, the ferroelectric BFO–PTO film exhibits a higher coercive field, as greater field strength is needed to induce polarization switching. Lowering the polarization frequency could alleviate this effect by allowing more time for domain alignment, but it would also increase leakage currents in the system, making it difficult to achieve the saturation of the ferroelectric polarization. Therefore, the position of the characteristic inflection points in the *P–E* loop and maxima in the *J–E* curve of this geometry is very close to the maximum applied field (Fig. 3). However, the BFO–PTO films deposited on Ni substrates with an LSMO layer display better defined ferroelectric hysteresis loops at room temperature (*P–E* loops and *J–E* curves), with distinctively lower coercive fields. This improvement is due to the no participation of the NiO layer in the capacitor, as LSMO serves as the bottom electrode (Table S1).

Notwithstanding the mechanism, the flexible sample formed by the BFO–PTO film on LSMO/Ni foil clearly exhibits the best ferroelectric response with a remanent polarization P_R of ~50 μC cm^{-2} and a coercive field (E_c) of 450 kV cm^{-2}. This P_R value is nearly equivalent to that of its ceramic counterpart, which is outstanding considering the differences in coercive field.[18] Additionally, note that such bulk-like performance of these flexible films is achieved after their solution processing at a temperature of only 500 °C, around 400 °C below

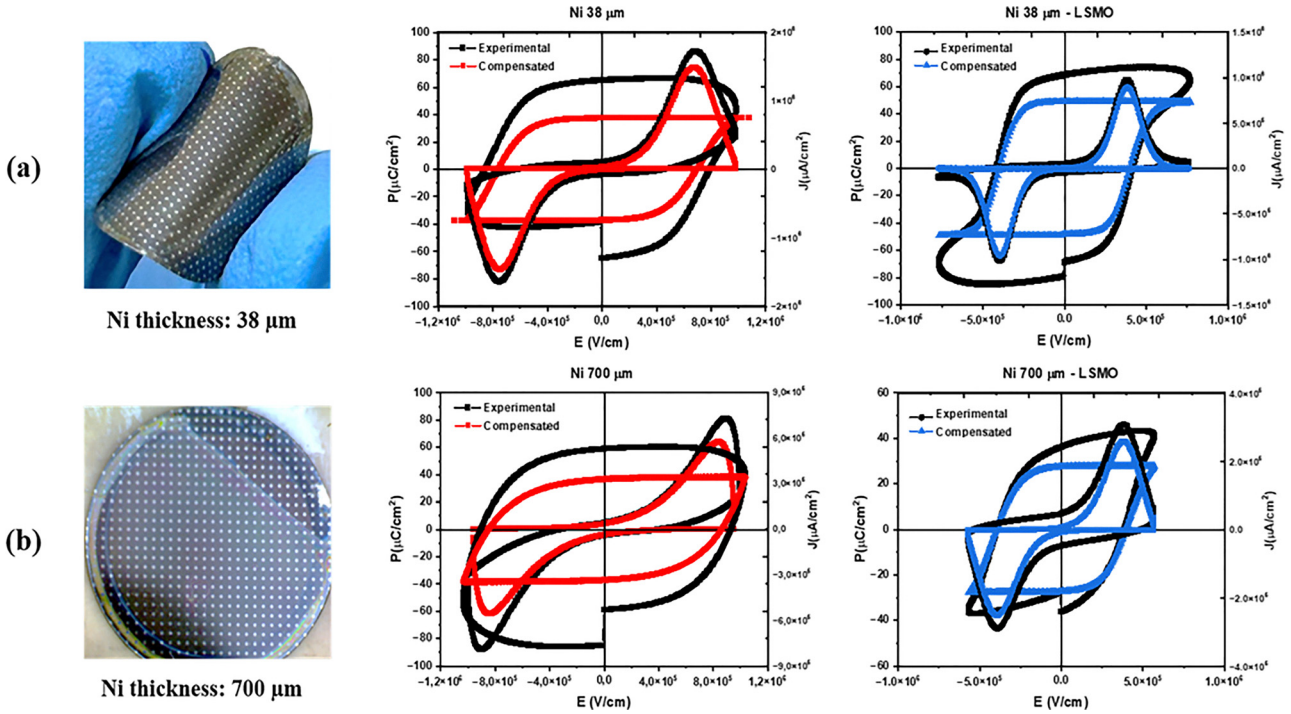

Fig. 3 Photographs, current curves and polarization hysteresis loops as a function of the applied electric field (J–E and P–E) for the BFO–PTO thin films deposited on: (a) 38 μm and (b) 700 μm Ni and LSMO/Ni substrates.

conventional processing temperatures for their counterpart bulk ceramics. Comparing the two sets of films, a significant improvement has been accomplished in terms of reduced leakage contribution and huge decrease in the coercive field at the maximum applied voltage (800 kV cm^{-2}) when the LSMO layer is introduced into the material heterostructure. The high remnant polarization, reduced leakage currents and low conduction losses make these designed composite film materials particularly suitable for applications requiring these characteristics, such as energy harvesters, for which flexibility is highly recommended. Table S1 summarizes the ferroelectric properties of these materials for solution-deposited BFO–PTO films on Ni substrates, both with and without the insertion of the LSMO as a buffer layer.

Energy harvesting applications of these bilayer composites requires the poling of the ferroelectric film with good polarization retention, which has been controlled with the pyroelectric response. Therefore, pyroelectric coefficients were calculated from dynamic pyroelectric measurements, performed after poling the planar capacitors of the samples with the maximum voltage achievable before dielectric breakdown occurred. An example is shown in Fig. 4a, where the pyroelectric current generated as a response to a triangular thermal wave is displayed. Consistently with the ferroelectric hysteresis loops, pyroelectric coefficients were one order of magnitude higher for the BFO–PTO films on LSMO/Ni than for those directly deposited on Ni without the LSMO buffer layer (8×10^{-9} C K^{-1} cm^{-2} and 6×10^{-10} C K^{-1} cm^{-2}, respectively). In addition, the pyroelectric response remains stable for longer times (at least up to 1 week) in the former case, indicating a better retention of polarization, which is a condition required to maintain an appropriate ME response of the device under in-operando conditions.[54]

Transverse ME coefficients, α_{31}, were obtained for the two different thicknesses of the Ni substrates, both without and with the insertion of the LSMO layer (Fig. 4b and c). Significantly lower coefficients were obtained in the structures without the LSMO interlayer. This is likely due to the combination of two effects: (i) the difficulty in achieving high remnant polarizations in the ferroelectric films directly deposited on Ni, due to their large coercive fields and associated low polarization retention, which limits the piezoelectric response of these films, and (ii) the deteriorated elastic coupling between the ferro-piezoelectric and magnetostrictive layers caused by interfacial secondary phases (primarily NiO). Both issues are resolved by the insertion of the LSMO buffer, which consequently leads to a significant increase in magnetoelectric coefficients.

Within each geometry, the highest ME voltage coefficients α_{31} are obtained for the samples deposited onto the 38 μm thick Ni foils. A maximum ME transverse output of $\alpha_{31} \sim 20$ mV cm^{-1} Oe^{-1} is obtained at a bias magnetic field (H_{DC}) of only 25 Oe, for the BFO–PTO film directly deposited on the Ni foil, whereas a much higher output of $\alpha_{31} \sim 40$ mV cm^{-1} Oe^{-1} is measured for the film on the LSMO/Ni sample at the same H_{DC}. The response could be further increased by enhancing the crystallinity of the ferroelectric film though a second RTP treatment at 600 °C. The ME coefficient increased from 40 mV cm^{-1} Oe^{-1} to 100 mV cm^{-1} Oe^{-1} after this treatment, as shown in Fig. 4d and e. These findings suggest that further optimization of crystallinity could lead to even greater improvements in ME properties, yet there must be a trade-off with the degradation of the elastic coupling.

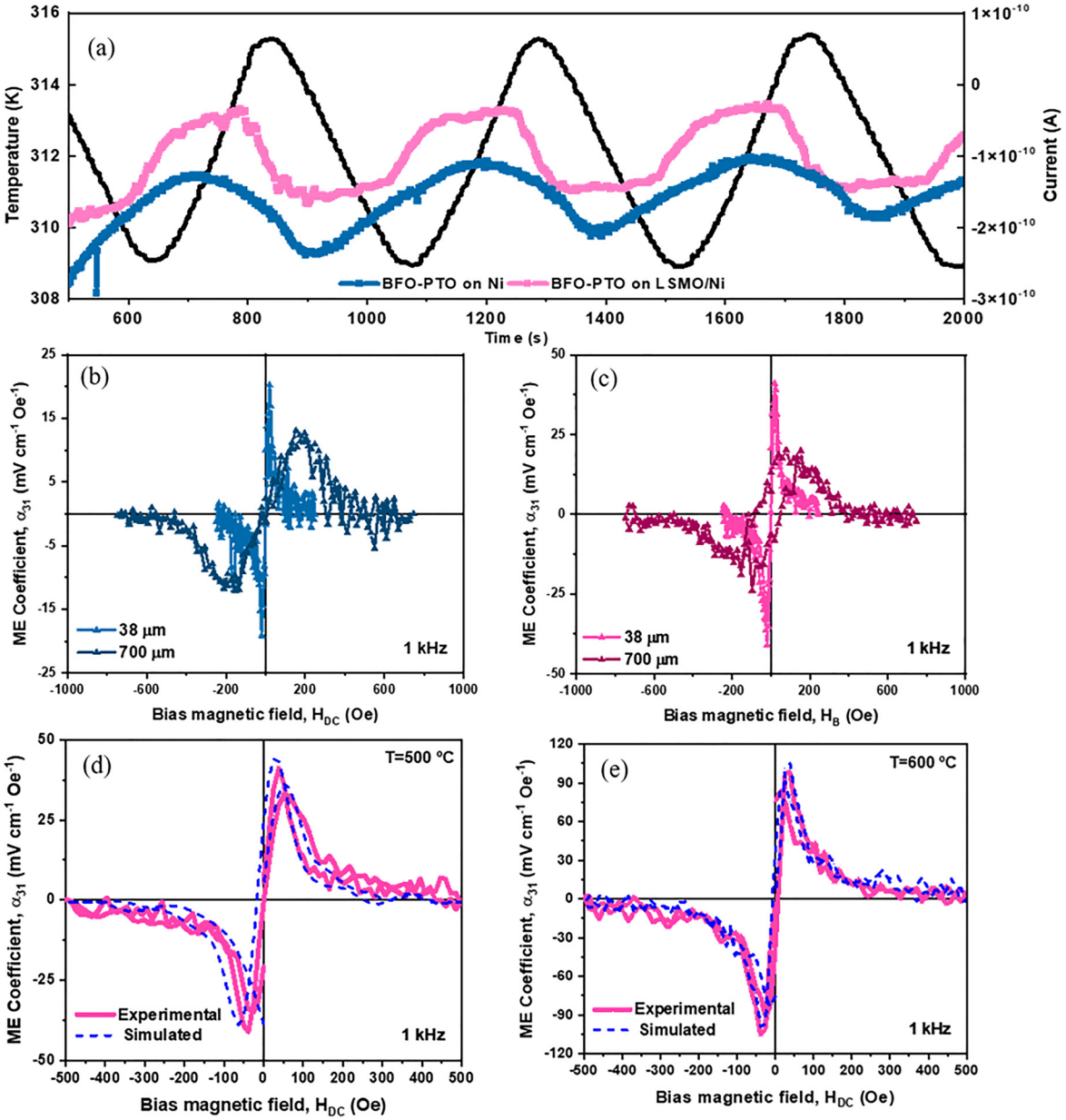

Fig. 4 (a) Pyroelectric measurements in the flexible BFO–PTO film on Ni foil and on LSMO/Ni foil, carried out after 48 hours of the film poling to show the retention of the polarization in these films. Pyroelectric current was measured with a thermo-stimulated current under an imposed triangular thermal wave. Transverse ME coefficients (α_{31}) obtained for the samples with the (b) BFO–PTO films directly deposited on Ni and (c) BFO–PTO films deposited on LSMO buffered Ni substrates. Experimental *vs.* calculated ME coefficient α_{31} obtained in BFO–PTO thin films on LSMO/Ni 38 μm foils and with the ferroelectric BFO–PTO film crystallized at (d) 500 °C and (e) 600 °C. Note the different *y*-scales in (b) and (c), and in (d) and (e).

Regarding the effect of substrate thickness, magnetoelectric coefficients distinctively decreased when Ni thickness was increased in both designs, at the same time that the field for maximum response shifted to higher values. The H_{DC} value at which α_{31} peaks are solely determined by the magnetostriction curve of the substrate, λ *vs.* H where λ is the strain and H is the magnetic field, and specifically by its derivative dλ/dH: the piezomagnetic coefficient q_{ij} that shows a characteristic maximum for a given H-value.[55] Results and trends observed in Fig. 4 can be discussed with the existing analytical solution for a two-layer structure, given in eqn (1), which provides a quick insight into how the different parameters influence the actual magnetoelectric coefficient.

$$\alpha_{31} = \frac{-k\nu(1-\nu)\left(q_{11}^{m} + q_{21}^{m}\right)d_{31}}{\varepsilon_{33}^{p}\left(s_{11}^{m} + s_{12}^{m}\right)k\nu + \varepsilon_{33}^{p}\left(s_{11}^{p} + s_{12}^{p}\right)(1-\nu) - 2kd_{31}^{2}(1-\nu)} \quad (1)$$

In this expression, the superscripts p and m refer to the piezoelectric and magnetostrictive phases, so that ε_{33} and d_{31} are the dielectric and piezoelectric coefficients of the ferroelectric component, while q_{ij} stands for the piezomagnetic coefficients

of the magnetic phase, and s_{ij} are the respective elastic compliances. Deviations from ideal elastic coupling are considered with factor k that ranges from 0 to 1. A last parameter in the formula is the composite component volume fraction, introduced as the volume of piezoelectric material relative to the total one, ν, which for equal areas, corresponds to the thickness ratio between the piezoelectric layer and total structure. For the thin film geometry, ν is typically <0.1 and the coefficient roughly increases linearly with the thickness ratio. This implies that reducing the substrate thickness must result in an increase of ME response as observed. This is also why most of the literature on analogous flexible systems have been focused on micrometric thick PZT films (film thickness well over the micron) on Ni foils and, subsequently, the ME coefficient increases accordingly (α_{31} values between 0.2 and 3 V cm^{-1} Oe^{-1}).[4,8,9,56,57] Besides, these structures have been predominantly fabricated by deposition techniques different from solution methods, in order to minimize the formation of NiO at the PZT/Ni interface, *e.g.*, pulsed laser deposition or plasma-enhanced atomic layer deposition. Albeit layered PZT/Ni flexible composites with high ME α_{31} coefficients were obtained in these cases, their fabrication was tedious and expensive, difficult to apply to the development of sustainable devices. Our solution-processed submicron-thick film reaches $\alpha_{31} \approx 100$ mV cm^{-1} Oe^{-1} at 25 Oe bias, matching state-of-the-art devices when the volume fraction parameter is taken into account.

Eqn (1) can be used to estimate the maximum magnetoelectric (ME) coefficient achievable in our composite material system. This estimation was done with literature-reported values for the material coefficients of BFO–PTO and Ni in bulk, which are collected in Table S2. This simulation leads to a maximum (ideal elastic coupling) theoretical α_{31} value of 580 mV cm^{-1} Oe^{-1} for the experimental υ-value of 0.013 in the flexible structure, which, if attained, it would be comparable to those reported for the quasi-2-2 multiferroic PZT/Pt/Ni film heterostructures.[58] The disagreement between the experimental α_{31} values and the theoretical ones could be attributed to various factors. One possible explanation is a deviation from ideal elastic coupling ($k < 1$). Hence, Fig. 5a shows data calculated from eqn (1) as a function of the thickness ratio υ assuming decreasing values for the coupling factor. This graph has allowed us to determine the k-value that corresponds to the experimental α_{31} of approximately 100 mV cm^{-1} Oe^{-1}. From it, an approximate value of $k = 0.33$ can be deduced, as this value results in a maximum theoretical α_{31} that aligns with the experimental result. This calculation assumes the piezoelectric coefficient of the ferroelectric layer is that taken from the literature, which corresponds to bulk ceramics (Table S2).[22] However, the reduction in the piezoelectric coefficients of ferroelectric perovskite oxide in thin film form is well-reported.[59] The eventual effect of a decreased piezoelectric

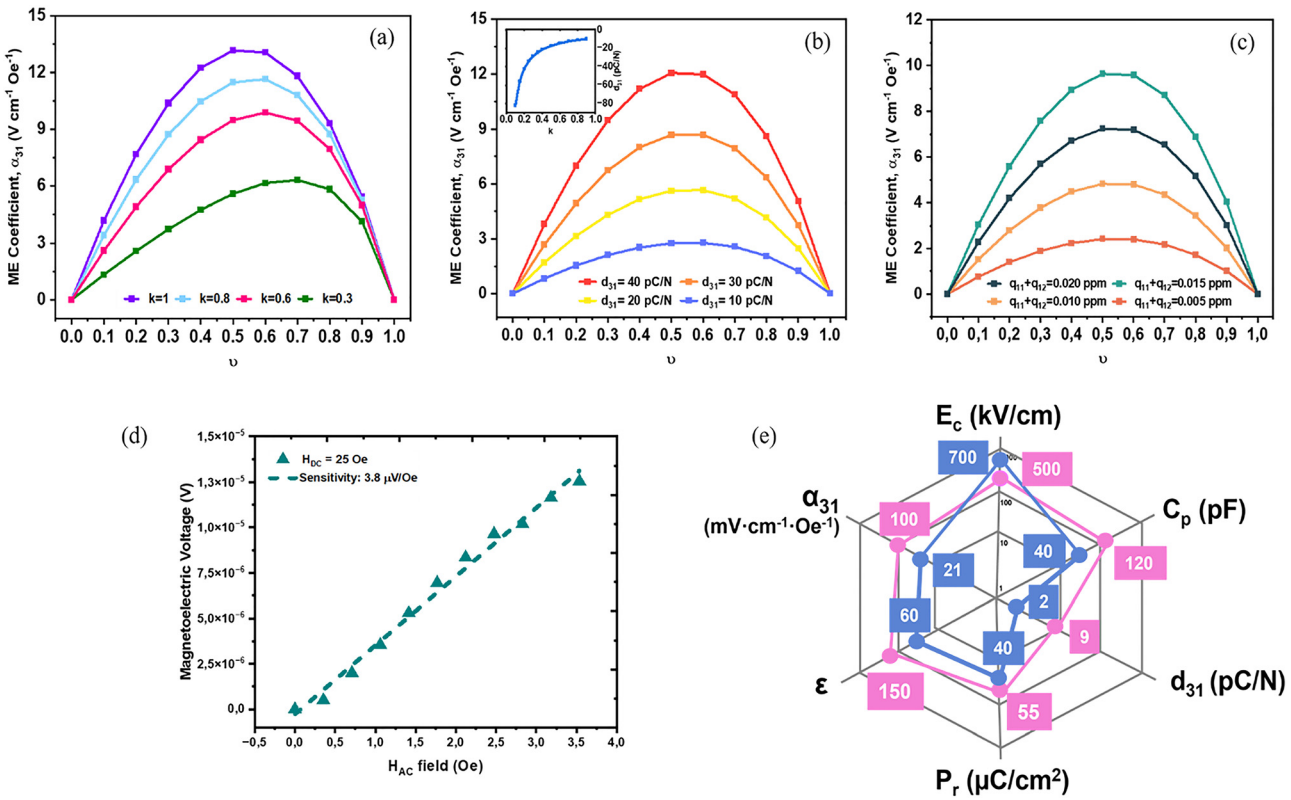

Fig. 5 Transverse magnetoelectric ME voltage dE_3/dH_1 as a function of the thickness ratio, ν, of the ferropiezoelectric and magnetostrictive components for (a) different interfacial coupling factors k, (b) various piezoelectric coefficients d_{31} and (c) multiple piezomagnetic coefficients $q_{11} + q_{12}$ scenarios. (d) Linear induced ME voltage *vs.* H_{AC} at a constant H_{DC} = 25 Oe. (e) Functional properties of the multiferroic flexible structure comparing the properties of the structures formed by the BFO–PTO film on Ni foil (blue) and that formed by the BFO–PTO film on LSMO/Ni foil (red).

coefficient is shown in Fig. 5b for ideal coupling. Once again, this curve allows a piezoelectric coefficient to be estimated from the experimental α_{31}. A value of 8.8 pC N^{-1} is obtained for $k = 1$, but this d_{31} would be higher if non-ideal coupling is assumed. Indeed, a curve of d_{31} as a function of k can be traced. Hence, a d_{31} of 17 pC N^{-1} is obtained for a more realistic situation with $k = 0.5$ (see the inset of Fig. 5b).

Although the previous discussion provides a rationale for the differences in the maximum magnetoelectric (ME) coefficient between the two designs of film-sample heterostructures, as well as the thickness effects, it does not clarify why the bias magnetic field corresponding to the maximum response shifts to higher values as the substrate thickness increases. Factors such as the composite component fraction, the interface, or the piezoelectric coefficients of the ferroelectric layer fail to account for this behavior. This phenomenon has been highlighted before and generically associated with demagnetization effects in the nickel substrate, and their well-known dependence on geometry.[8,9] However, a comprehensive description of how this affects the magnetostriction and thus, piezomagnetic coefficients of the magnetic metal substrates has not been provided. Roughly speaking, magnetization curves, *M vs. H*, of a square plate change with aspect ratio, L/t, where L and t are lateral dimension and thickness, respectively, so that the initial slope, *i.e.* susceptibility, increases with L/t, though the final saturation magnetization is always the same. Magnetostriction is proportional to the square of magnetization; therefore, the saturation magnetostriction is not expected to change. However, the shape of the curve does change, which affects its derivative, *i.e.*, the piezomagnetic coefficient. This effect for nickel plates with the two aspect ratios employed in this work has been simulated using Comsol Multiphysics by means of procedures explained in the SI, where obtained magnetostriction curves and piezomagnetic coefficients are also given for the two substrates. Note that not only the field for maximum piezomagnetic coefficient clearly increases as aspect ratio decreases, but the value of the piezomagnetic coefficient also changes, significantly decreasing with it. Values of 0.8 ppm and 0.25 ppm at 25 Oe and 83 Oe bias fields are obtained for the 38 and 700 μm-thick Ni substrates, respectively.

The actual measurements might not be accurate, since the same magnetic susceptibility, saturation magnetization, and magnetostriction have been assumed for all the Ni substrates. Nevertheless, coherent trends are observed, indicating that piezomagnetic coefficients must vary with the Ni thickness. This clearly complicates estimating the expected magnetoelectric coefficients with eqn (1), because strong variation with piezomagnetic coefficients is anticipated as illustrated in Fig. 5c. Therefore, magnetostriction was experimentally measured for each of the two round substrates with a diameter of 1.5 mm and different thicknesses of 38 μm and 700 μm. These results are given in the SI. These measurements provided experimental values for the piezomagnetic coefficients as a function of the bias magnetic field (Fig. S7), which allows the full magnetoelectric curves to be obtained with eqn (1) for all the possible υ ratios. The latter curves are shown in Fig. 5a–c, assuming bulk d_{31} values and the k-factor that gives the correct maximum magnetoelectric coefficient. Note the excellent agreement between the experimental data and the curve obtained using the equation and the experimental magnetostriction curves.

These results indicate that substrate thinning is a powerful means of increasing the magnetoelectric response of the studied thin film composite structures. This is not only a consequence of the increased ferroelectric volume fraction, but also of the minimization of demagnetization effects of the Ni substrate. As a consequence, the flexible sample ($\sim$38 μm thick Ni foil substrate) has an optimized magnetoelectric response, in principle capable of detecting, or converting into usable electrical power, small magnetic stimuli present in different environments and inaccessible at larger scales. As shown in Fig. 5d, the ME voltage exhibits a clear linear dependence on the amplitude of the AC magnetic field H_{AC}, where the slope (3.8 μV Oe^{-1}) would represent the sensitivity of a hypothetical sensor. This linear relationship is crucial for precise and reliable sensing performance, where consistent and predictable response is essential.[60,61]

Throughout this work, the significance of the different parameters that influence the magnetoelectric response of a magnetoelectric thin film composite fabricated by solution deposition of a ferroelectric film on a magnetic substrate has been analyzed. Understanding the importance of these factors is crucial for optimizing the performance of the device, with the final aim of obtaining flexible structures. By utilizing low-temperature solution deposition methods, along with a ferroelectric perovskite system with stable properties on downscaling, we have been able to fabricate a magnetoelectric heterostructure that not only maintains the required properties of the single piezoelectric and magnetostrictive components, but also provides good elastic coupling between them, and allows flexible structures to be obtained. As summarized in Fig. 5e, significant improvement in the functional properties of the system is obtained with the introduction of the LSMO perovskite as an interfacial buffer between the ferro-piezoelectric film and the magnetostrictive substrate. The inclusion of this buffer enhances the ferroelectric properties of the film and its elastic coupling with the magnetic substrate, leading to an enhanced magnetoelectric response. Examining the characteristic values of the ferroelectric system individually, it becomes clear how the use of LSMO interlayers contributes to improving the overall performance and efficiency of the system. In addition, flexible structures based on thinned substrates are shown to provide enhanced performance by the synergetic effects of increased ferroelectric fraction and a minimized demagnetization field. This advancement brings us closer to the goal of utilizing these devices for energy harvesting applications, where flexibility, efficiency, and cost-effectiveness are key.

3. Experimental section

3.1. Preparation of the BFO–PTO/Ni heterostructures

3.1.1. Magnetic nickel (Ni) substrates. Ni substrates with two different thicknesses of 700 μm and 38 μm were used in

this study. All of them were purchased from Goodfellow, but their geometry and characteristics changed according to commercial availability. They were as follows: (i) 700 μm thick Ni discs of ∅ = 15 mm, not polished and (ii) 38 μm thick Ni foil discs of ∅ = 15 mm, not polished. These Ni substrates were polished using Al_2O_3 polishing slurries with decreasing particle size from 9 down to 1 μm, in order to homogenize surface characteristics and reduce the roughness of the two substrates. The surfaces of the substrates were measured using a Taylor Hobson Form Talysurf 50 mm Intra 2 profilometer, performing 400 scans over 8 × 8 mm areas. The average roughness (R_a) was ≤20 nm. These values confirm that the polishing procedure yielded a smooth and uniform surface suitable for subsequent thin film deposition. Two different types of experiments were conducted to compare the effect of the interface. The first set of experiments involved the direct deposition of films onto nickel substrates, with decreasing thickness. In the second set, the films were also deposited on Ni substrates with decreasing thickness, but with a LSMO-buffered interface layer, as described in the following sections.

3.1.2. Ferroelectric $0.65BiFeO_3$–$0.35PbTiO_3$ (BFO–PTO) films. Precursor solutions with nominal compositions of $0.65BiFeO_3$–$0.35PbTiO_3$ (BFO–PTO) in the proximity of the morphotropic phase boundary (MPB), were prepared by adapting a procedure previously published, in which the BFO and PTO sols were separately synthesized and mixed.[19,62,63] The precursors were diluted in dried ethanol to achieve an equivalent concentration of 0.1 mol L^{-1}. These solutions were then spin-coated on the substrates at 2000 rpm for 45 s. The wet layers were dried at 100 °C for 5 min, pyrolyzed at 250 °C for 5 min and crystallized at 500 °C for 10 min by rapid thermal processing (RTP, JIPELEC, JetStar 100T Processor) in oxygen at a heating rate of ∼30 °C s^{-1}. The deposition, drying, pyrolysis and crystallization steps were successively repeated a minimum of ten times to achieve films with a thickness of ∼500 nm (Fig S3a and S4).

3.1.3. $La_{0.7}Sr_{0.3}MnO_3$ (LSMO) buffer layer. $La(CH_3COO)_3 \cdot 3H_2O$, $Sr(CH_3COO)_2$ and $Mn(CH_3COO)_3 \cdot 4H_2O$ reagents were separately dissolved in an excess of propionic acid (C_2H_5COOH) and the corresponding propionate salts ($C_9H_{18}LaO_6$, $C_6H_{10}O4Sr$ and $C_6H_{10}MnO_4$) were precipitated in each of the solutions by adding acetone ($(CH_3)_2CO$). The precipitated powders were filtered and washed with distilled water and dried at 100 °C overnight. Stoichiometric amounts of the lanthanum, strontium and manganese propionates were dissolved together in propionic acid to obtain a precursor solution of $La_{0.7}Sr_{0.3}MnO_3$ (LSMO) with an equivalent concentration of 0.3 mol L^{-1}. The solution was diluted to 0.1 mol L^{-1} by adding a mixture of 1-butanol (C_4H_9OH) and propionic acid in a 1 : 1 molar ratio. This LSMO solution was spin-coated on the substrates at 4000 rpm for 45 s.[64] The wet layers were dried at 100 °C for 5 min, pyrolyzed at 250 °C for 5 min and crystallized at 500 °C for 10 min by RTP in oxygen at a heating rate of ∼30 °C s^{-1}. The deposition, drying, pyrolysis and crystallization steps were successively repeated five times to obtain 250 nm films. Then, the crystallization of the LSMO perovskite film was achieved at 600 °C for 10 min, using RTP in an oxygen atmosphere and with a heating rate of ∼30 °C s^{-1} (Fig. S3b). A resistivity of 3.2 mΩ cm of an LSMO ∼15 nm thick film deposited on a strontium titanate ($SrTiO_3$) substrate was measured with a KeithleySourcemeter using a four-point probe configuration with Ag contacts.

The thickness of the different layers across the functional heterostructures was measured by a Taylor Hobson Form Talysurf 50 mm Intra 2 profilometer, on step-edges deliberately left uncoated, and confirmed on cross-section specimens by SEM. The NiO that forms during thermal processing is located at the Ni/film interface, making it difficult to obtain an accurate measurement by this means. Nevertheless, depth-profile XPS carried out in a previous publication from our group required ≈300 min of Ar-ion sputtering to saturate the Ni signal.[17] Using the calibrated sputter rate of the spectrometer (≈2 nm min^{-1}), this corresponds to an interfacial NiO thickness of roughly 100 nm.

3.2. Characterization of the BFO–PTO/Ni heterostructures

3.2.1. Crystal structure of the BFO–PTO films. Perovskite structure was examined using X-ray diffraction (XRD) analysis conducted with a Bruker D8 Advance apparatus equipped with a Cu anode stage (λ = 1.5418 Å). For high resolution diffractograms, grazing incidence X-ray diffraction (GI-XRD) experiments were carried out at The Materials Science and Powder Diffraction beamline BL04-MSP in ALBA Synchrotron at the Powder Diffraction End Station, which is equipped with a three-circle goniometer. The outer and middle circles support respectively the high angular resolution multi analyzer detection (MAD) setup and the high-throughput position sensitive detector (PSD) MYTHEN. The inner circle is equipped with an Eulerian goniometer on which all sample environments are mounted. Measurements were carried out with a micrometric spot size, which varied depending on the incidence angle (2.5–5°), with a photon beam working at 22 keV (λ = 0.5636 Å).

Crystal structure was further investigated by Raman spectroscopy. A Bruker Senterra confocal Raman microscope system (developed by Bruker Optik GmbH, Ettlingen, Germany) was used to perform this material characterization. This apparatus integrates a high-resolution laser confocal microscope, excited at a wavelength of λ = 532 nm. The system laser was focused onto the sample surface, producing a spot size of approximately 1 μm in diameter. These measurements mapped the samples surface and were performed from 50 to 1000 cm^{-1} with an exposure time of 30 s.

3.3. Functional properties of the BFO–PTO/Ni heterostructures

3.3.1 Ferroelectric characterization. For the electrical measurements, an array of parallel capacitors was fabricated by depositing on the film surfaces circular 20 nm thick Pt electrodes with ∅ ∼ 200 μm by electron-beam physical vapor deposition through a shadow mask. The capacitors were then annealed by RTP at 350 °C for 10 min to improve the film/electrode electric

contact. Current density (*J–E*) curves were measured at room temperature (RT) using a HP 8116A function generator to apply sinusoidal waves with frequencies of 500 Hz, 1 kHz and 2 kHz. The current response under the applied voltage was first amplified with a Keithley 428 current amplifier, and then collected with a Tektronix (TDS 520) oscilloscope. Ferroelectric hysteresis loops were obtained by integrating the *J–E* curves. Non-switching effects (leakage currents and conductivity) were calculated and subtracted from the experimental hysteresis loop by a fitting procedure that simulates the linear contributions with the capacitance and resistance of the films, as well as nonlinear leakage contributions.[65]

3.3.2 Poling and pyroelectric characterization. Films were poled at room temperature (RT) utilizing voltage-biased sine waves at a frequency of 1 kHz. Positive and negative poling of different capacitors were achieved by altering the signal polarity in the sample holder. Pyroelectric characterization was conducted to comparatively assess poling levels and control the remanence of the films. A dynamic technique was employed, involving the measurement of thermo-stimulated current (TSC) generated by a low-frequency thermal wave slightly above room temperature, followed by analysis to identify any pyroelectric contribution. Temperature triangular waves with a 6 K amplitude and heating/cooling rates of ± 3 K min^{-1} were applied, while currents were measured using a Keithley 6514 System Electrometer. These measurements were carried out on the circular electrodes with a diameter of 200 μm, thus being the estimated capacitor area of $\sim 3.14 \times 10^{-2}$ mm^2.

3.3.3. Magnetoelectric characterization. The experimental set-up shown in Fig. S1 in the SI was used for the magnetoelectric characterization of the materials prepared in this work after their poling. It consists of two Helmholtz coils designed to simultaneously provide a high-power static magnetic field up to 1 kOe (for the magnetic biasing of the material) and an alternating magnetic field with amplitude in the range from 1 to 10 Oe with frequency between 1 kHz and 10 kHz (the stimulus). The ME output voltage (response) was then recorded using a lock-in amplifier (SignalRecovery model 7265) as a function of the bias field. Magnetic fields were applied within the film plane, and voltage measurements were conducted across the film thickness, from the top electrodes to the Ni substrate, so that the transverse voltage coefficient α_{31} was obtained as the bias magnetic field was increased in steps.

4. Conclusions

Solution-processed, lead-less content $0.65BiFeO_3$–$0.35PbTiO_3$ (BFO–PTO) ferro-piezoelectric thin films have been directly integrated at low temperatures with magnetostrictive Ni plates and foils to explore their potential as magnetoelectric (ME) energy harvesters. The roles of the piezoelectric and magnetostrictive volume fraction (ν), the elastic coupling between the film and substrate, the poling level of the ferroelectric film, and the demagnetization effects in the metal substrate were individually analyzed to optimize these parameters for high-sensitivity energy harvesting. By maintaining a constant piezoelectric layer thickness in the sub-micron range (≤ 500 nm) and varying the Ni thickness from the millimeter scale (Ni plates) to the micrometer range (Ni foil), a significant improvement in the magnetoelectric coefficient was achieved. This improvement results from the synergistic effects of the ferroelectric fraction and the enhanced piezomagnetic coefficients due to minimized demagnetization fields. Additionally, this study highlights the critical role of interfacial engineering in enhancing ME thin-film device performance. The adverse effects of the inevitable NiO interlayer, common in these materials, were mitigated by introducing a $La_{0.7}Sr_{0.3}MnO_3$ (LSMO) buffer layer between the BFO–PTO film and Ni. This LSMO layer, also solution-deposited at low temperature, served as a bottom electrode and promoted the crystallization of the BFO–PTO ferroelectric film, resulting in enhanced ferroelectric responses, with remnant polarizations, P_R of approximately 50 μC cm^{-2}, approaching bulk-like values. The elastic coupling between the piezoelectric (~ 500 nm thick BFO–PTO film) and magnetostrictive (Ni foil) components was facilitated by the LSMO buffer layer, achieving coupling factors of at least $k \sim 0.33$. Magnetoelectric coefficient values ($\alpha_{ME} \sim 100$ mV cm^{-1} Oe^{-1}) were measured in optimized ferroelectric films on Ni foils after electrical poling and under a bias magnetic field (H_{DC}) of only 25 Oe. A linear response was observed with H_{AC} within the 1–10 Oe range. Although these α_{ME} values are lower than theoretically predicted for the piezoelectric/magnetostrictive component ratio (ν), the reduction likely arises from non-ideal elastic coupling and decreased d_{31} coefficients in thin-film form. Nevertheless, the flexible magnetoelectric materials fabricated here using cost-effective, low thermal-budget procedures demonstrate excellent magnetic field sensing capabilities, achieving a sensitivity of 3.8 μV Oe^{-1}. These findings emphasize the importance of optimizing the ferroelectric fraction, poling level, magnetic substrate geometry, and interface quality in achieving high magnetoelectric responses. The results demonstrate the potential of thin-film flexible structures and scalable fabrication techniques for magnetoelectric energy harvesting applications.

Author contributions

Investigation, methodology, writing original draft, A. B.; investigation, methodology, validation, writing review and editing, R. J.; software, validation, writing review and editing, P. R.; investigation, methodology, validation, writing review and editing, H. A.; investigation, methodology, writing review and editing, I. B.; project administration, conceptualization, funding acquisition, investigation, methodology, supervision, validation, writing original draft, M. A.; project administration, conceptualization, funding acquisition, investigation, methodology, supervision, validation, writing original draft, writing review and editing, M. L. C.

Conflicts of interest

There are no conflicts to declare.

Data availability

The data that support the findings of this study are available from the corresponding authors upon request.

Supplementary information is available. Additional results from this study are provided in the Supplementary Information. See DOI: **https://doi.org/10.1039/d5tc02144h**.

Acknowledgements

This work was funded by the Spanish Projects TED2021-130871BC21, PID2022-136790OB-I00, PID2021 and CNS2022-135743 projects, funded by MCIN/AEI/10.13039/501100011033 and the European Union ''NextGeneration EU''/PRTR.

Notes and references

1 Y. Liu, L. Wang, L. Zhao, X. Yu and Y. Zi, *InfoMat*, 2020, **2**(2), 318–340.
2 X.-K. Wei, N. Domingo, Y. Sun, N. Balke, R. E. Dunin-Borkowski and J. Mayer, *J. Adv. Energy Mater.*, 2022, **12**(24), 2201199.
3 W. Eerenstein, N. D. Mathur and J. F. Scott, *Nature*, 2006, **442**(7104), 759–765.
4 R. Gupta, M. Tomar, V. Gupta, Y. Zhou, A. Chopra, S. Priya, A. S. Bhalla and R. Guo, *Energy Harvesting Systems*, 2016, **3**(2), 181–188.
5 N. Ortega, A. Kumar, J. F. Scott and R. Katiyar, *J. Phys.: Condens. Matter*, 2015, **27**, 504002.
6 A. Bagri, A. Jana, G. Panchal, S. Chowdhury, R. Raj, M. Kumar, M. Gupta, V. R. Reddy, D. M. Phase and R. J. Choudhary, *ACS Appl. Mater. Interfaces*, 2023, **15**(14), 18391–18401.
7 Y. Zhang, C. R. Bowen, S. K. Ghosh, D. Mandal, H. Khanbareh, M. Arafa and C. Wan, *Nano Energy*, 2019, **57**, 118–140.
8 H. Palneedi, D. Maurya, L. D. Geng, H. C. Song, G. T. Hwang, M. Peddigari, V. Annapureddy, K. Song, Y. S. Oh, S. C. Yang, Y. U. Wang, S. Priya and J. Ryu, *ACS Appl. Mater. Interfaces*, 2018, **10**(13), 11018–11025.
9 H. Palneedi, H. G. Yeo, G.-T. Hwang, V. Annapureddy, J. W. Kim, J.-J. Choi, S. Trolier-McKinstry and J. Ryu, *APL Mater.*, 2017, **5**(9), 096111.
10 H. Palneedi, D. Maurya, G.-Y. Kim, V. Annapureddy, M.-S. Noh, C.-Y. Kang, J.-W. Kim, J.-J. Choi, S.-Y. Choi, S.-Y. Chung, S. J. L. Kang, S. Priya and J. Ryu, *Adv. Mater.*, 2017, **29**(10), 1605688.
11 A. Dmitriyeva, V. Mikheev, S. Zarubin, A. Chouprik, G. Vinai, V. Polewczyk, P. Torelli, Y. Matveyev, C. Schlueter, L. Karateev, Q. Yang, Z. Chen, L. Tao, E. Y. Tsymbal and A. Zenkevich, *ACS Nano*, 2021, **15**(9), 14891–14902.
12 M. I. Bichurin, V. M. Petrov and G. Srinivasan, *Phys. Rev. B: Condens. Matter Mater. Phys.*, 2003, **68**(5), 054402.
13 N. A. Spaldin, *Science*, 2004, **304**(5677), 1606–1607.
14 S. S. Won, H. Seo, M. Kawahara, S. Glinsek, J. Lee, Y. Kim, C. K. Jeong, A. I. Kingon and S. H. Kim, *Nano Energy*, 2019, **55**, 182–192.
15 I. Bretos, R. Jiménez, J. Ricote and M. L. Calzada, *Chem. Soc. Rev.*, 2018, **47**(2), 291–308.
16 J. Koruza, A. J. Bell, T. Frömling, K. G. Webber, K. Wang and J. Rödel, *J. Materiomics*, 2018, **4**(1), 13–26.
17 H. Amorín, M. Venet, J. E. García, D. A. Ochoa, P. Ramos, J. López-Sánchez, J. Rubio-Zuazo, A. Castro and M. Algueró, *Adv. Electron. Mater.*, 2024, **10**(2), 2300556.
18 M. Algueró, L. Zia, R. Jiménez, H. Amorín, I. Bretos, A. Barreto, G. H. Jaffari, E. Rodríguez-Castellón, P. Ramos and M. L. Calzada, *APL Energy*, 2023, **1**(3), 036108.
19 L. J. Zia, G. H. Jaffari, R. Jiménez, I. Bretos, H. Amorín, M. Algueró, E. Rodríguez-Castellón and M. L. Calzada, *J. Am. Ceram. Soc.*, 2022, **105**(2), 888–900.
20 M. Algueró, H. Amorín, T. Hungría, J. Galy and A. Castro, *Appl. Phys. Lett.*, 2009, **94**(1), 012902.
21 H. Amorín, C. Correas, P. Ramos, T. Hungría, A. Castro and M. Algueró, *Appl. Phys. Lett.*, 2012, **101**(17), 172908.
22 H. Amorín, C. Correas, C. M. Fernández-Posada, O. Peña, A. Castro and M. Algueró, *J. Appl. Phys.*, 2014, **115**(10), 104104.
23 W. Liang, Y. Ji, T. Nan, J. Huang, Z. Bi, H. Zeng, H. Du, C. Chen, Q. Jia and Y. Lin, *ACS Appl. Mater. Interfaces*, 2012, **4**(4), 2199–2203.
24 W. Liang, Z. Li, Z. Bi, T. Nan, H. Du, C. Nan, C. Chen, Q. Jia and Y. Lin, *J. Mater. Chem. C*, 2014, **2**(4), 708–714.
25 B. Chen, N. N. Su, W. L. Cui and S.-N. Yan, *Phys. Lett. A*, 2018, **382**(16), 1124–1130.
26 S. Sharma, S. Gupta, R. Gupta, H. Borkar, A. Kumar, V. Gupta and M. Tomar, *ECS J. Solid State Sci. Technol.*, 2021, **10**, 071001.
27 J.-J. Choi, J. Ryu, B.-D. Hahn, W.-H. Yoon, B.-K. Lee, J.-H. Choi and D.-S. Park, *J. Am. Ceram. Soc.*, 2010, **93**(6), 1614–1618.
28 R. Kambale, D. Patil, J. Ryu, Y. Chai, K. Kim, W.-H. Yoon, D.-Y. Jeong, D.-S. Park, J.-W. Kim, J.-J. Choi and C.-W. Ahn, *J. Phys. D: Appl. Phys.*, 2013, **46**, 092002.
29 H. G. Yeo and S. Trolier-McKinstry, *J. Appl. Phys.*, 2014, **116**(1), 014105.
30 A.-P. Wang, G. Song, F.-P. Zhou, L.-N. Zhao, M. Jin, M. Liu, Y. Zhang, L.-I. Hu, J. Qi, H. Xu and M. Feng, *J. Mater. Sci.: Mater. Electron.*, 2021, **32**(5), 5920–5927.
31 G. Srinivasan, E. Rasmussen, B. Levin and R. Hayes, *Phys. Rev. B: Condens. Matter Mater. Phys.*, 2002, **65**, 134402.
32 Y. Meng, S. B. Lu and J. Gao, *Adv. Mater. Res.*, 2012, **460**, 214–217.
33 C. Thiele, K. Dörr, O. Bilani, J. Rödel and L. Schultz, *Phys. Rev. B: Condens. Matter Mater. Phys.*, 2007, **75**(5), 054408.
34 J.-B. Yau, X. Hong, A. Posadas, C. H. Ahn, W. Gao, E. Altman, Y. Bason, L. Klein, M. Sidorov and Z. Krivokapic, *J. Appl. Phys.*, 2007, **102**(10), 103901.
35 X. Han, Y. Ji, L. Wu, Y. Xia, C. R. Bowen and Y. Yang, *Nano-Micro Lett.*, 2022, **14**(1), 198.
36 M. L. Calzada, R. Jiménez, A. González and J. Mendiola, *Chem. Mater.*, 2001, **13**(1), 3–5.

37 D. Pérez-Mezcua, R. Sirera, R. Jiménez, I. Bretos, C. De Dobbelaere, A. Hardy, M. K. Van Bael and M. L. Calzada, *J. Mater. Chem. C*, 2014, **2**(41), 8750–8760.
38 D. Pérez-Mezcua, I. Bretos, R. Jiménez, J. Ricote, R. J. Jiménez-Rioboó, C. G. da Silva, D. Chateigner, L. Fuentes-Cobas, R. Sirera and M. L. Calzada, *Sci. Rep.*, 2016, **6**(1), 39561.
39 I. Bretos, R. Jiménez, J. Ricote and M. L. Calzada, *IEEE Trans. Ultrason. Eng.*, 2020, **67**(10), 1967–1979.
40 I. Bretos, S. Diodati, R. Jiménez, F. Tajoli, J. Ricote, G. Bragaggia, M. Franca, M. L. Calzada and S. Gross, *Chem. – Eur. J.*, 2020, **26**(42), 9157–9179.
41 Z. Duan, X. Shi, Y. Cui, Y. Wan, Z. Lu and G. Zhao, *J. Alloys Compd.*, 2017, **698**, 276–283.
42 R. Jiménez, J. Ricote, I. Bretos, R. J. Jiménez Riobóo, F. Mompean, A. Ruiz, H. Xie, M. Lira-Cantú and M. L. Calzada, *J. Eur. Ceram. Soc.*, 2021, **41**(6), 3404–3415.
43 R. J. Zeches, M. D. Rossell, J. X. Zhang, A. J. Hatt, Q. He, C. H. Yang, A. Kumar, C. H. Wang, A. Melville, C. Adamo, G. Sheng, Y. H. Chu, J. F. Ihlefeld, R. Erni, C. Ederer, V. Gopalan, L. Q. Chen, D. G. Schlom, N. A. Spaldin, L. W. Martin and R. Ramesh, *Science*, 2009, **326**(5955), 977–980.
44 M. Branescu, C. Naudin, M. Gartner and G. Nemeş, *Thin Solid Films*, 2008, **516**(22), 8190–8194.
45 D. Sando, Y. Yang, E. Bousquet, C. Carrétéro, V. Garcia, S. Fusil, D. Dolfi, A. Barthélémy, P. Ghosez, L. Bellaiche and M. Bibes, *Nat. Commun.*, 2016, **7**(1), 10718.
46 F. Fan, B. Luo, M. Duan and C. Chen, *J. Appl. Spectrosc.*, 2013, **80**(3), 378–383.
47 Y. Yang, Y. J. Y. Sun, K. Zhu, Y. L. Liu and L. Wan, *J. Appl. Phys.*, 2008, **103**(9), 093532.
48 A. Mijiti, M. Mamat, F. Xiaerding, Q. Wang, A. Abudurexiti and L. Aihaiti, *Mater. Res. Express*, 2021, **8**(3), 036408.
49 J. A. Sanjurjo, E. López-Cruz and G. Burns, *Phys. Rev. B: Condens. Matter Mater. Phys.*, 1983, **28**(12), 7260–7268.
50 A.-D. Li, D. Wu, C.-Z. Ge, P. Lü, W.-H. Ma, M.-S. Zhang, C.-Y. Xu, J. Zuo and N.-B. Ming, *J. Appl. Phys.*, 1999, **85**(4), 2146–2150.
51 J. Yao, W. Ge, L. Luo, J. Li, D. Viehland and H. Luo, *Appl. Phys. Lett.*, 2010, **96**(22), 222905.
52 M. A. Khan, T. P. Comyn and A. J. Bell, *Appl. Phys. Lett.*, 2007, **91**(3), 032901.
53 Y. Huang, Z. Yin and Y. Xiong, *J. Appl. Mech.*, 2010, **77**(4), 041016.
54 Y. Guo, C. Yang and B. Huang, *Energies*, 2023, **16**(13), 1–19.
55 E. Klokholm and J. Aboafl, *J. Appl. Phys.*, 1982, **53**(3), 2661–2663.
56 A. B. Swain, M. Rath, S. Dinesh Kumar, M. S. Ramachandra Rao, V. Subramanian and P. Murugavel, *J. Phys. D: Appl. Phys.*, 2019, **52**(6), 065004.
57 T. Nguyen, Y. Fleming, P. Bender, P. Grysan, N. Valle, B. El Adib, N. Adjeroud, D. Arl, M. Emo, J. Ghanbaja, A. Michels and J. Polesel-Maris, *ACS Appl. Mater. Interfaces*, 2021, **13**(26), 30874–30884.
58 M. Feng, J. J. Wang, J.-M. Hu, J. Wang, J. Ma, H. B. Li, Y. Shen, Y.-H. Lin, L.-Q. Chen and C.-W. Nan, *Appl. Phys. Lett.*, 2015, **106**(7), 072901.
59 J. F. Ihlefeld, D. T. Harris, R. Keech, J. L. Jones, J.-P. Maria and S. Trolier-McKinstry, *J. Am. Ceram. Soc.*, 2016, **99**(8), 2537–2557.
60 Y. W. Lee, J. Y. Soh, I. R. Yoo, J. Cho, C. W. Ahn, J. J. Choi, B. D. Hahn and K. H. Cho, *Sensors*, 2020, **20**, 6635.
61 D. Arora, P. Kumar and D. Kaur, *ACS Appl. Electron. Mater.*, 2024, **6**(3), 1959–1970.
62 Y. L. Tu, M. L. Calzada, N. J. Phillips and S. J. Milne, *J. Am. Ceram. Soc.*, 1996, **79**(2), 441–448.
63 C. Gutiérrez-Lázaro, I. Bretos, R. Jiménez, J. Ricote, H. E. Hosiny, D. Pérez-Mezcua, R. J. Jiménez Rioboó, M. García-Hernández and M. L. Calzada, *J. Am. Ceram. Soc.*, 2013, **96**(10), 3061–3069.
64 P. Machado, M. Scigaj, J. Gazquez, E. Rueda, A. Sánchez-Díaz, I. Fina, M. Gibert-Roca, T. Puig, X. Obradors, M. Campoy-Quiles and M. Coll, *Chem. Mater.*, 2019, **31**(3), 947–954.
65 S. L. Miller, R. D. Nasby, J. R. Schwank, M. S. Rodgers and P. V. Dressendorfer, *J. Appl. Phys.*, 1990, **68**(12), 6463–6471.